Model of Microalloy Precipitation during Continuous Casting and Reheating

[1]Kun Xu, Brian G. Thomas
Mechanical Science and Engineering Department
University of Illinois at Urbana-Champaign
1206 West Green St. Urbana, IL 61801, USA
Phone - (217) 333-6919
Email - kunxu2@illinois.edu, bgthomas@illinois.edu

[2]Myra S. Dyer, John G. Speer, David K. Matlock
George S. Ansell Department of Metallurgical and Materials Engineering
Advanced Steel Processing and Products Research Center
Colorado School of Mines
1500 Illinois St. Golden, CO 80401, USA
Phone - (303) 273-3025
Email - mdyer@mines.edu, jspeer@mines.edu, dmatlock@mines.edu

Key words: Niobium, Precipitate Formation, Continuous Casting, Temperature, Equilibrium, Kinetic, Particle-Size-Grouping Models

ABSTRACT

A comprehensive set of models of precipitate formation during steel processing has been developed. In this work, it is applied to investigate Nb(C,N) precipitation in thin microalloyed steel slabs during continuous casting, reheating in a tunnel furnace and water quenching relative to the position with the slab and alloy content. The models include a transient heat-conduction and solidification model of temperature evolution (CON1D), a multi-component equilibrium model of precipitate phase stability to compute the supersaturation, and a Particle-Size-Grouping (PSG) model to simulate the quantities, compositions, and size distributions of the precipitates as they evolve throughout the process. The results are compared with measurements conducted on steel samples obtained from the commercial plant. New insights into precipitate formation during hot-charging are presented.

INTRODUCTION

Due to their excellent strength, toughness and weldability, high strength low alloy (HSLA) steels have many applications including pipeline, construction, transportation and automotive industries [1]. HLSA steels typically contain less than 0.2% carbon, up to 2% manganese and small amounts (<0.1%) of niobium, titanium and vanadium. The carbide and nitride precipitates which form during rolling of HSLA steels retard austenite grain growth and recrystallization and thereby encourage grain refinement, precipitation hardening, and improved mechanical properties [2]. Small additions of niobium are particularly effective at forming small Nb(C,N) precipitates which presumably act by solute drag [3-5] and pinning of austenite grain boundaries [6-8].

Precipitation can also lead to crack formation during other processing stages such as the casting of these steels [9,10]. If large numbers of fine precipitate particles accumulate along weak grain boundaries at elevated temperatures, they may cause local voids, which concentrate strain at grain boundaries, decrease ductility and cause cracks. Thus, the composition, shape, size distribution and volume fraction of these Nb(C,N) precipitates are all very important to determine engineering performance of HSLA steels [11].

Precipitation of Nb(C,N) in undeformed austenite is very slow in typical microalloyed steels. It can take 15-30 min for precipitation to start, and around 1 day to finish [12]. This precipitation is greatly accelerated by 10-1000 times with deformation strain, such as occurs during controlled rolling. This is because the dislocation density is highly increased and the dislocations serve as precipitation nucleation sites and diffusion paths [4,5]. Precipitation is also hastened by the $\gamma \rightarrow \alpha$ phase transformation because of the increased diffusion rate and decreased solubility of these precipitates in ferrite, which are well documented for AlN precipitation [13,14]. Many studies have been done to understand the effects of niobium precipitation on austenite recrystallization during hot-rolling, the kinetics of niobium precipitation during casting and reheating processes [15-17], and the effects of niobium precipitation and thermomechanical processing on the mechanical properties of HSLA steels [18]. Niobium carbonitride is also mutually soluble with titanium and vanadium carbonitrides, as all of these precipitates have f.c.c. crystal structures and similar lattice parameters [2]. Thus,

mixed precipitates form in reality [19,20], making niobium precipitation more important and complex. There is a strong need to predict the dynamic formation of precipitates, including their composition, morphology and size distribution, as a function of processing conditions.

Previous work [17,21] investigated niobium precipitation and dissolution after continuous casting of typical Nb-containing HSLA steels and after reheating at different positions within a thin slab (i.e. thermal profile of the slab). This research aims to build on that study by simulating and measuring niobium precipitate size distributions in one of those HSLA steels. This work is the next step in the development of a comprehensive, fundamentally-based system of models to predict temperature, important microstructural features such as precipitation and grain size, properties such as ductility and strength, and defects such as crack formation during steel processing.

Objectives

The purpose of this paper is to present an efficient, fundamental new model of precipitate formation during steel processing developed at the University of Illinois, and to apply it to simulate niobium precipitation during continuous casting, reheating and quenching of thin-slab samples of HSLA steel measured at Colorado School of Mines [17,21]. The first step uses the solidification heat transfer model, CON1D [22], to predict the temperature and steel phase histories during the process, for the conditions experienced by the slab samples. Next, an equilibrium precipitation model is used to predict the maximum amounts and compositions of the precipitates experienced at every temperature of the process. Finally, a kinetic model is used to predict the evolving amounts and size distributions of the Nb(C,N) precipitates. The predictions are compared with the measured precipitate fractions and size distributions. This powerful method has a broad range of potential applications in predicting precipitate evolution during thermal processing of microalloyed steels. This work takes another step towards the fundamental prediction and prevention of problems such as transverse cracking due to locally high temperature, large grains and embrittling precipitates.

HEAT TRANSFER MODEL

Temperature and phase fraction evolution during the solidification, casting and reheating process is the first crucial part of a model system to predict microstructure and ductility. In this work, the transient heat conduction equation is solved in the mold, spray regions, reheating furnace and quenching water of a continuous steel slab caster using the CON1D program [22]. This finite-difference model calculates one-dimensional heat transfer within the solidifying steel shell coupled with two-dimensional steady-state heat transfer in the mold and a careful treatment of the interfacial gap between the shell and mold. Below the mold, the model includes the temperature and spatially-dependent heat transfer coefficients of each spray nozzle, according to the local water flow rates, and the heat extraction into each support roll [23]. After exiting the last spray zone, subsequent reheating or quenching stages can be added by restarting the simulation using an "initial" temperature profile from any desired previously-calculated time. A non-equilibrium microsegregation model, based on an analytical Clyne-Kurz equation developed by Won and Thomas [24], was applied to compute the liquidus temperature, solidus temperature and steel phase fractions. Complete details of CON1D are provided elsewhere [22].

EQUILIBRIUM PRECIPITAION MODEL

A thermodynamic analysis is the first step of precipitation prediction. An equilibrium precipitation model has been developed to predict precipitation of 18 kinds of oxides, sulfides, nitrides and carbides typically found in microalloyed steels [25]. The model calculates the amounts of each precipitate phase at equilibrium, and their compositions for the given steel grade and temperature. These results also represent the supersaturation needed for the following kinetic calculation.

The model solves a fully-coupled system of 35 solubility-product equations by Newton-Raphson iteration for the amounts and compositions of each precipitate SiO_2, TiS, $Ti_4C_2S_2$, AlN, BN, Cr_2N and/or mutually-soluble precipitate group $TiNbV(CN)$, $AlTi(O)$, $MnMg(O)$, $MnMg(S)$. For example, the temperature-dependent equilibrium solubility product, K, for dissolved atoms of elements M and X to give a solid precipitate of compound M_xX_y is:

$$K_{M_xX_y} = a_M^x \cdot a_X^y / a_{M_xX_y} \tag{1}$$

For the low solute contents of the steels of interest in this work, the activity a_i, of each element i, (wt%) is defined using Henry's law as follows:

$$a_i = \gamma_i[\%i] \text{ where } \log_{10}\gamma_i = \sum_{j=1}^{13} e_i^j[\%j] \tag{2}$$

where γ_i is the activity coefficient, e_i^j is the Wagner interaction coefficient of element i as affected by alloying element j, and $[\%i]$ is the dissolved mass concentration of element i (wt%).

The activities of precipitates which are mutually exclusive, existing separately from other precipitates, remain at unity. On the other hand, mutually soluble precipitates always appear together as a mixed group with variable composition. Their activities are assumed to be given by their respective fractions in the mixed precipitate, and the sum of the activities of the precipitates that comprise a mutually soluble group is unity. Mutual solubility between precipitates is a consequence of their similar crystal structures and lattice parameters.

The solubility limit of each precipitate in each steel phase (liquid, ferrite and austenite) is satisfied simultaneously by iteration, including updated Wagner interactions, while also conserving the mass of each alloying element. Convergence can be aided by systematically solving the system at all temperatures, starting at a high temperature when all precipitates are dissolved, and using each solution as an initial guess for the next, slightly lower temperature. The model has been validated with analytical solutions of simple precipitation cases. The predictions match reasonably well with several sets of previous experimental measurements, including examples using the commercial package, JMat-Pro. Further details of the equilibrium precipitation model are given elsewhere [25].

TRANSIENT PRECIPITATION MODEL

Precipitates can form at different rates, stages and locations during steel processing, including in the liquid steel due to rapid diffusion and collisions, the mushy-zone between dendrites and grains due to rapid diffusion in the segregated liquid, and in the solid state due to slow diffusion inside the grains, or faster diffusion at the grain boundaries. These different mechanisms cause the precipitate particles to show a variety of compositions, morphologies and size distributions. The formation rate of precipitates may be very sluggish even if they are thermodynamically favored. Thus, a kinetic model to describe the precipitation rate under non-equilibrium conditions, and to quantify the evolution of the particle size distribution with time, is essential to make realistic predictions, especially for carbonitride precipitates in microalloyed steels.

Most previous models separate precipitation into different stages, which include nucleation, growth, and coarsening. Different equations are developed for each stage with many assumptions, simplifications, and empirical parameters. The mean particle size is simulated, instead of the actual size distribution. The nucleation stage includes an induction period to form stable nuclei, followed by steady-state nucleation [26]. After nucleation, particles of all sizes can grow due to the high supersaturation that drives the growth stage [27]. After the nucleation and growth stages, precipitates of various sizes are dispersed in the matrix phase. Once the supersaturation decreases to equilibrium, the solute concentrations in the matrix and at the particle/matrix interface are comparable and capillary effects become dominant, causing coarsening or Ostwald ripening [28]. Governed by the minimization of the total surface energy, coarsening is driven by the difference in concentration gradients near precipitate particles of different sizes. The larger particles are surrounded by low concentration, so grow by diffusion from the high concentration surrounding smaller particles, which are less stable and shrink. Thus, the net number density of all particles now decreases with time. Further details on nucleation [29], growth [30] and coarsening [31] are given elsewhere.

An efficient new numerical model based on solving population balances with the Particle-Size-Grouping (PSG) method has been developed to simulate nonequilibrium precipitate formation during processing of realistic multi-component microalloyed steels with reasonable computer execution times. The model can predict the evolution of precipitate amounts, size distributions, and compositions for a given temperature history. It includes nucleation, growth and coarsening stages in a general way.

The new model uses Kampmann's approach [32] because it includes the different mechanisms which govern the nucleation, growth and coarsening stages into a single model, without explicitly splitting the behavior into discrete stages. The stages naturally evolve according to the changing dominant mechanism. The model simulates diffusion growth, and dissociation, including the influence of minimization of surface energy and supersaturation based on the equilibrium model. The number densities of every particle size are tracked through the entire simulation. The only model parameters are material properties with physical significance, and include the diffusion coefficients and interfacial energies. The governing population balance equations are [32]

$$\frac{dn_i}{dt} = -\beta_i n_1 n_i + \beta_{i-1} n_1 n_{i-1} - \alpha_i A_i n_i + \alpha_{i+1} A_{i+1} n_{i+1} \quad (i \geq 2) \tag{3}$$

where n_1, n_{i-1}, n_i, n_{i+1}: Number density of size *1* ,*i*-1, *i* and *i*+1 particles ($\#\cdot m^{-3}$)
β_i : Diffusion growth rate constant of size *i* particles ($m^3 \cdot \#^{--1} \cdot s^{-1}$)
α_i : Dissociation rate per unit area of size *i* particles ($m^{-2} \cdot s^{-1}$)
A_i : Reaction area of size *i* particles (m^2)

The first and second terms on the right of equation (3) quantify the loss and generation of size *i* particles due to diffusion, while the third and fourth terms give the loss and generation of size *i* particles due to dissociation. The diffusion and dissociation rates are found from [32].

$$\beta_i = 4\pi D r_i ,\ \alpha_i = \frac{\beta_i}{A_i} n_{1,eq} \exp\left(\frac{2\sigma V_P}{RT} \frac{1}{r_i} \right) \tag{4}$$

where D : Diffusion coefficient of single pseudomolecules in steel ($m^2 \cdot s^{-1}$)
r_i : Radius of size i particles (m)
$n_{1,eq}$: Number density of the dissolved pseudomolecules at equilibrium ($\# \cdot m^{-3}$)
σ : Interfacial tension between the precipitate and steel ($J \cdot m^{-2}$)
V_P : Molar volume of the precipitate ($m^3 \cdot mol^{-1}$)
R : Ideal gas constant ($8.314 J \cdot K^{-1} \cdot mol^{-1}$)
T : Absolute temperature (K)

Practical models of precipitate growth must simulate particle sizes ranging from a single "pseudomolecule", which is an "embryo" or stoichiometric cluster of atoms consisting of as few as a single metallic/interstitial atom pair (~0.1nm) to large coarsened precipitate particles (~100μm). These particles contain from ~1 to ~10^{18} pseudomolecules, which makes the computation impossible for any method based on a linear size scale. In order to overcome this difficulty, the Particle-Size-Grouping (PSG) method is adopted. This method has been shown to be accurate and effective for modeling particle collisions [33]. The original PSG method divides the entire wide range of particle sizes into a small number of size groups, with a characteristic size for each size group. Starting from single pseudomolecules, it can cover the entire realistic size range by taking advantage of the tremendous power of logarithmic scales. For example, by doubling the size of each successive group, the 1-10^{18} range can be covered with only 60 groups. Instead of calculating the interactions between particles of every size, the PSG method considers interactions only between size groups and within size groups and calculates the number densities of size groups.

Recently, a new PSG method with better accuracy for diffusion problems has been developed by tracking border values adjacent to the size group boundaries [34]. The population balance equations for this new PSG method are as follows:

$$\begin{aligned} \frac{dN_j}{dt} = & \frac{m_1}{m_j} \beta_j N_1 (N_j - n_j^R) - \frac{m_1}{m_j} \alpha_j A_j (N_j - n_j^L) \\ & + \frac{ceil(m_{j-1,j})}{m_j} \beta_{j-1}^R N_1 n_{j-1}^R + \frac{floor(m_{j,j+1})}{m_j} \alpha_{j+1}^L A_{j+1}^L n_{j+1}^L \\ & - \frac{floor(m_{j,j+1})}{m_j} \beta_j^R N_1 n_j^R - \frac{ceil(m_{j-1,j})}{m_j} \alpha_j^L A_j^L n_j^L \quad (j \geq 2) \end{aligned} \tag{5}$$

where n_j^L is the number density of those particles in size group j which fall into size group j-1 by losing one pseudomolecule, and n_j^R is the number density of those particles in size group j which jump into size group j+1 by gaining one pseudomolecule. m_j, $m_{j-1,j}$ and $m_{j,j+1}$ are the number of pseudomolecules contained at the center and boundaries inside size group j. Function *ceil* calculates the smallest integer which is not less than the given real number, and *floor* gives the largest integer which is not larger than the given real number. In Eq. (5), the first and second terms on the right account for diffusion growth and dissociation inside size group j, and the third and fourth terms account for the generation of size group j particles by inter-group diffusion growth and dissociation. The last two terms quantify the loss of size group j particles due to the diffusion growth and dissociation of size group j particles themselves. The "border values" of number densities between adjacent size groups are carefully modeled to obtain good accuracy, and an implicit scheme is applied to solve the equations, in order to the computationally-intensive small time steps required to satisfy the stability requirements of explicit methods [34].

With this new method, the mass balance is strictly satisfied, and a good match with exact solutions has been found. The model has been validated with measured precipitation fractions and size distributions in several plant and laboratory experiments found in previous literature. Further details on the model and its validation are given elsewhere [34].

EXPERIMENTS

A 1200mm×50mm thin slab of HSLA steel was continuously cast at Nucor-Steel-Hickman at a speed of 5.0m/min. This "High-Nb" steel (as designated in the prior publication [21]) had weight composition of 0.031% C, 1.039% Mn, 0.194% Si, 0.031% Ni, 0.032% Cr, 0.01% Mo, 0.003% Ti, 0.046% Nb, 0.001% V, 0.031% Al, 0.006% N, 0.003% S, 0.012% P. The mold working length was 850mm, and the water spray cooling zones spanned from mold exit to 6m below the meniscus. The typical recorded slab surface

temperature was 800°C at exit from the last support roll in the spray zone. The slab then traveled a few meters past a cutoff shear, and was hot charged at ~980°C surface temperature into a several-hundred-meter-long reheating furnace with an internal temperature of 1080°C.

The slab samples were full-width crops of ~700mm length taken either at the shear or prior to the hot-rolling mill. Each cropped steel sample was rapidly quenched in agitated water to room temperature, and cut into small pieces, 300mmx125mmx50mm. The samples were first dissolved in two stages to separate and measure the precipitated Nb from the Nb in solution. Then, the precipitates were counted in selected sections and compositions were measured to determine the size distributions of Nb-bearing precipitates.

Electrochemical extraction and inductively coupled plasma atomic emission spectrometry (ICP-AES) techniques were used to quantify the amounts of niobium in solution and precipitate form. Three different volumes were cut from each slab sample and identified as chill zone near the slab surface/edge (S), columnar zone at medium depth (M), and equiaxed zone near the slab center (C), as shown in Figure 1. Three different trial heats were tested, containing low, medium, or high niobium additions, and with similar levels of carbon, manganese, silicon, aluminum and nitrogen. Each steel specimen was dissolved in an aqueous solution of 5% hydrochloric acid and 3% tartaric acid and filtered to separate the dissolved steel matrix from the alloy precipitate. The precipitate residue and filter papers were then dissolved in a second solution prior to chemical analysis. After chemical extraction and precipitate dissolution, each solution was diluted with deionized water prior to ICP-AES. The sum of the two niobium amounts (in solution and precipitated) gives the total niobium measured. Good reproducibility was found, to demonstrate accuracy of the experiments [17].

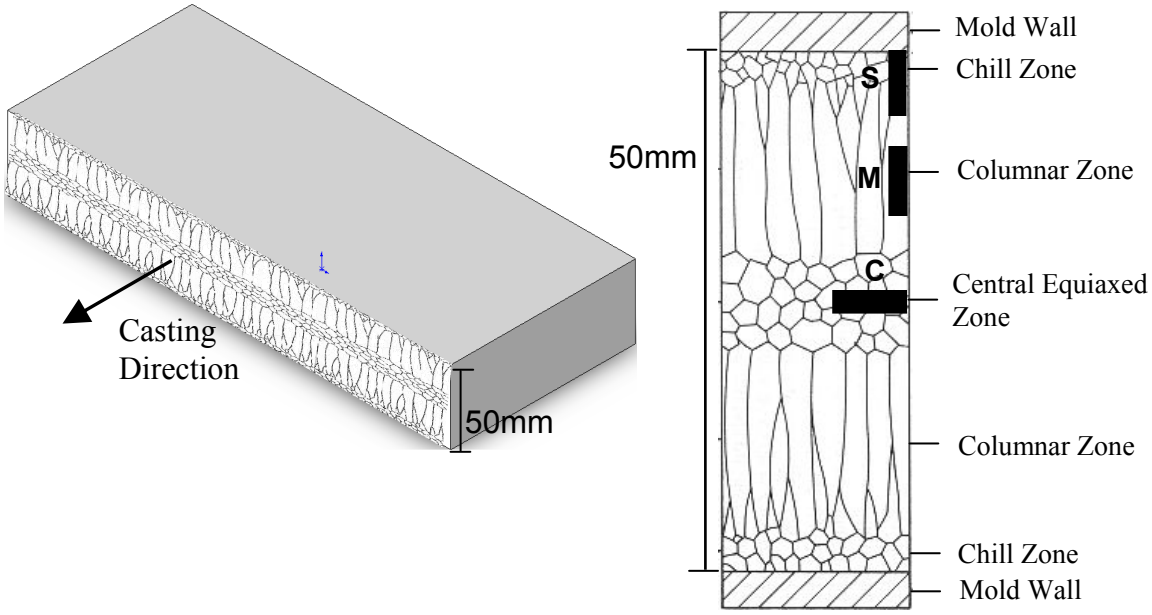

Figure 1: Solidification regions and sample orientations within continuous cast thin slab [17, 21]

The precipitate size distributions and compositions were then measured by transmission electron microscopy (TEM) and energy dispersive spectroscopy (EDS) on carbon extraction replicas from selected samples. A typical precipitate particle distribution for the high-Nb steel at the furnace exit that is measured and modeled in this work is shown in Figure 2. The experiments showed that the extent of precipitation increased with increasing niobium addition. The most niobium precipitation occurred at the slab surface along the edges of the thin slab, where dissolution subsequently occurs during reheating and equalization in the tunnel furnace. The columnar region comprised the bulk of the slab volume, and exhibited minimal alloy segregation and the lowest amount of precipitated niobium. The slab edge exhibited relatively small (10-30nm) irregular-cuboidal and cuboidal precipitates, and the columnar and centerline regions contained larger irregular-cuboidal and cuboidal precipitates. Further details on these experiments are provided elsewhere [17, 21].

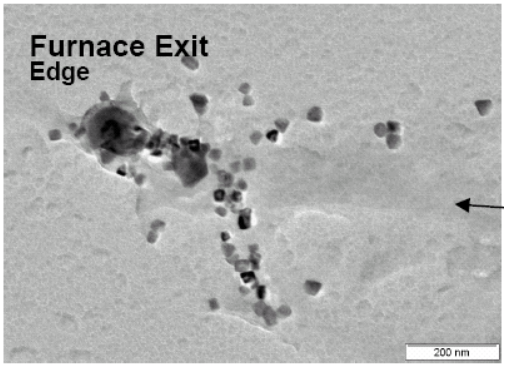

Figure 2: TEM analysis of Nb(C,N) precipitates in the slab edge/surface sample quenched after reheat furnace exit [17]

RESULTS

The measurements and model predictions are presented here for the high-Nb steel sample. The surface/edge (S), middle/columnar (M) and center (C) locations in the experiments are chosen as 0mm, 12.5mm and 25mm from the slab surface in the simulation. The modeling procedure follows the steps outlined in the objective section.

Heat Transfer

The solidification heat transfer code, CON1D is used to predict the temperature and steel phase histories. The pouring temperature is assumed to be 1553°C. Starting with the heat transfer coefficient boundary conditions of [23], the water spray heat transfer rates were adjusted in order to match the recorded caster exit temperature of 800°C and tunnel furnace entry temperature of 980°C. A "restart run" is performed to continue reheating of the sample in the tunnel furnace and quenching in agitated water. Natural convection with air is taken as $8.7 W \cdot m^{-2} \cdot K^{-1}$, and the heat transfer coefficient for the agitated water is $2000 W \cdot m^{-2} \cdot K^{-1}$.

Figure 3 shows the calculated equilibrium steel phase evolution with temperature, and it follows as liquid→ δ ferrite→ austenite→ α ferrite (and Fe_3C) with decreasing temperature. The predicted temperature histories inside the slab are shown in Figure 4. At the slab surface, the temperature decreases quickly in the mold and water spray cooling zones. Surface temperature increases after exiting the caster due to heat supplied from the slab interior, which tends to equilibrate the temperature distribution. Temperature decreases again slightly due to air cooling, prior to entering the reheating furnace. After an initial increase, temperature stays constant through most of the reheating furnace, and sharply decreases when the cropped sample is water quenched. In the slab interior, as half thickness and center, the temperature decreases slowly in the mold and water spray cooling zone, and continues to decrease due to air cooling after the caster. Like the surface, internal temperature increases to a constant in the reheating furnace, and finally sharply decreases by water quenching.

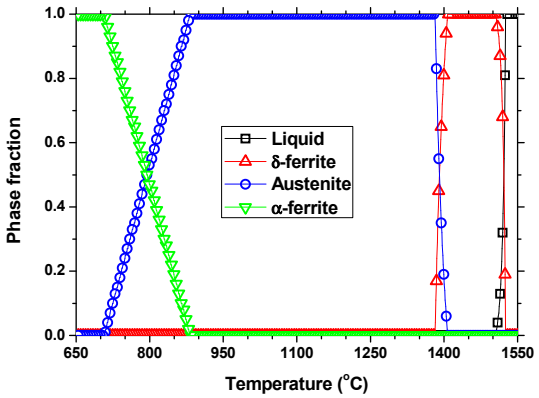

Figure 3: Evolution of phase fractions with temperature for experimental steel

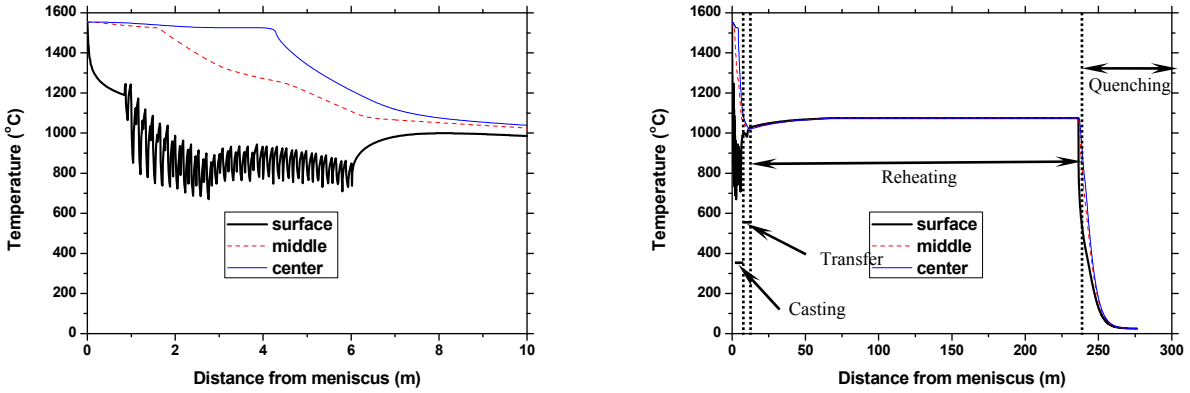

Figure 4: Calculated temperature history in caster region (left) and reheat furnace (right)

Equilibrium Precipitation

The equilibrium precipitation model is used to predict equilibrium phases as a function of temperature, based on the given steel composition and matrix phases from the heat transfer model. The results are graphed in Figure 5 for the matrix phase fractions in Figure 3. Solubility products and Wagner interaction coefficients for the δ-ferrite and austenite are tabulated elsewhere [25], and the effect of the small amount (<0.4%) of Fe_3C is ignored.

For this steel, MnS starts to precipitate at 1508°C in δ-ferrite, and then partly dissolves during the δ-ferrite to austenite transformation because the solubility limit of MnS is higher in austenite than ferrite. This is consistent with experimental observations of large sulfide precipitates, which were not included in the size distributions counted in the next section. With decreasing temperature, (Ti,Nb,V)(C,N) precipitates from 1289°C and AlN precipitates from 1039°C in austenite as shown in Figure 5(a). The precipitation of AlN is delayed by the formation of (Ti,Nb,V)(C,N) because part of its required nitrogen has been consumed. The equilibrium dissolved mass concentration of niobium, which is represented as [Nb], is also shown in the figure. These data are input into the transient precipitation model as $n_{1,eq}$ in Eq. (4). Figure 5(b) also shows the composition changes expected in the mixed (Ti,Nb,V)(C,N) precipitates. At high temperature, TiN is the most thermodynamically stable compound, so the mixed precipitates are mainly TiN according to the thermodynamic model employed for these calculations. With decreasing temperature, more carbides form as they become stable and there is much more carbon than nitrogen in steel. Interestingly, the NbN fraction increases, then decreases, with lowering temperature, reaching a maximum at ~1050°C. Below 650°C, NbC comprises over 86% of the (Ti,Nb,V)(C,N). The fractions of TiC, VN and VC are always small because these compounds are relatively less stable.

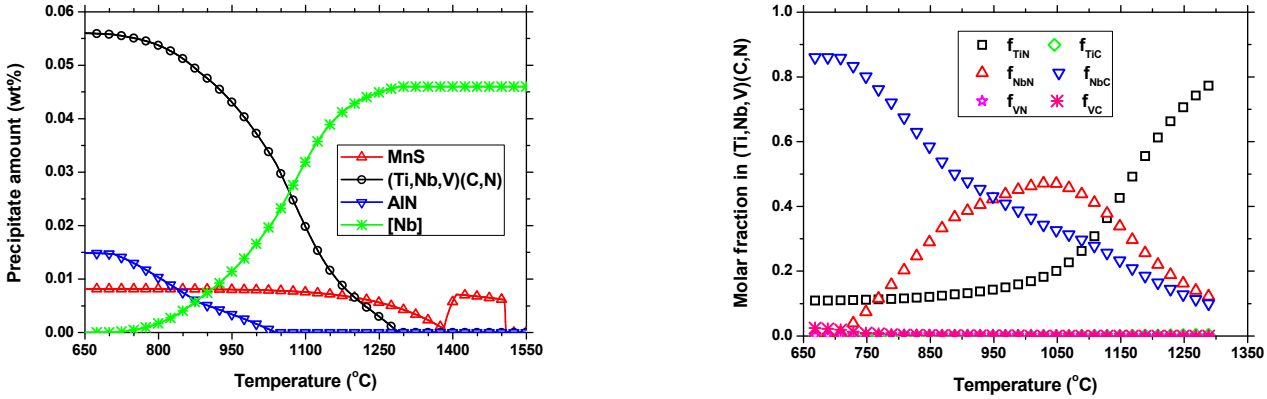

(a). Precipitate amount

(b). Molar fractions in (Ti,Nb,V)(C,N)

Figure 5: Equilibrium precipitation calculation results

Transient Precipitation

Results from the heat transfer and equilibrium models are used in the transient precipitation model to predict the evolving size distributions of Nb(C,N) in the measured samples. For this work on Nb precipitation in microalloyed steel, the diffusion coefficient is based on phase fraction according to a crude mixture rule, $D=f_\gamma D_\gamma+f_\alpha D_\alpha$, where $D_\gamma(m^2\cdot s^{-1})=0.83\times10^{-4}\exp(-266500/RT)$ in austenite and $D_\alpha(m^2\cdot s^{-1})=50.2\times10^{-4}\exp(-252000/RT)$ in ferrite [35]. While this assumption is crude, it only has an influence in the small

temperature ranges where the matrix is undergoing transformation. The effect of the small amount of Fe_3C is neglected. The interfacial energy between Nb(C,N) and the steel matrix is taken to be constant $0.5 J \cdot m^{-2}$ as a first approximation.

The calculated amounts of precipitated niobium during casting, transfer, reheating, and quenching of the thin-slab samples are shown in Figure 6. The predictions match well with the experimental measurements in the final quenched samples. The precipitate diameter used to define the size distributions is truncated at 4nm, according to the estimated resolution limit of the electrochemical extraction experiment. At the slab surface, Nb(C,N) starts to precipitate during the casting stage and reaches a maximum at the end of spray cooling. This Nb(C,N) then mainly redissolves, due to the reheating from the slab interior. A tiny peak is observed near the end of the transfer stage, owing to a slight cooling of the surface prior to entering the reheat furnace. In the reheating furnace, Nb(C,N) continues to dissolve due to the increasing temperature, as expected. Finally, the precipitated Nb reaches a constant amount, as equilibrium is approached. In the slab interior, there is almost no Nb(C,N) precipitation predicted until after reheating and quenching, due to the austenite to α-ferrite transformation during quenching. Because the slab center is cooled slower than the columnar region during quenching, more niobium precipitated in the slab center. During the quenching stage, the center precipitates most, columnar next and surface least, owing to the decreasing growth times at these 3 locations.

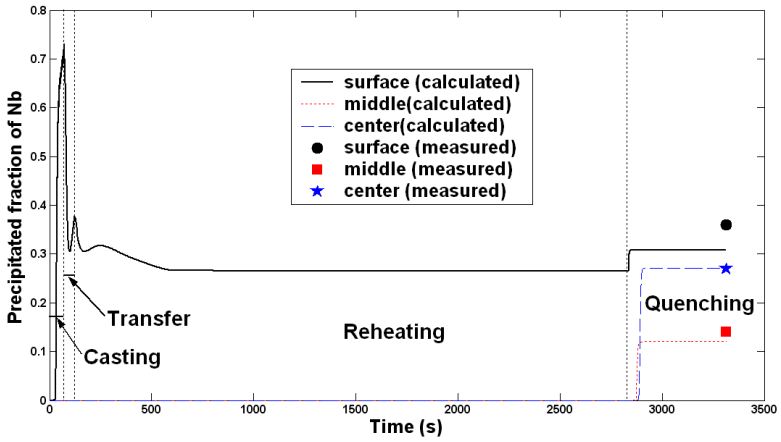

Figure 6: Calculated and measured precipitated fraction of Nb of slab

The calculated particle size distributions prior to the reheating furnace, at the end of the reheating furnace, and after quenching are shown in Figure 7. During casting, the precipitates are not stable, so their number density is a maximum for (dissolved) single pseudo-molecules (~0.35nm) and decreases exponentially with increasing particle diameter. The critical particle size for stable nucleation is interpreted as the minimum in the curves, because smaller particles tend to shrink and larger ones tend to grow. At the slab surface, large particles continue to grow and small particles begin to dissolve during the reheating stage, which clearly shows the effect of coarsening. In the slab interior, the particles are not predicted to grow much until the quenching stage, when the sharp increase can be explained by the austenite to ferrite transformation. With much higher diffusion rate and lower solubility limit, the precipitation of Nb(C,N) is expected to be greatly accelerated during this phase transformation.

The calculated and measured size distributions of Nb-bearing particles are compared in Figure 8. The calculated particle size is clearly much smaller than the measurements. The prediction comes closest at the surface (edge), where the mean predicted particle size of 11nm compares with the measured mean of 24nm, and the distribution shape is similar. The measurements show that particle size consistently increases with distance from surface (edge), to middle (columnar) to centerline regions. The calculation fails to show this trend. Segregation likely causes local enrichment of the solute concentration field during solidification, which is greater towards the slab interior.

A segregation model including back diffusion in the solid phase [24] is used to compute the segregated concentrations of alloying elements during solidification, and the result are shown in Figure 9. The segregation concentrations at solid fraction f_s=0.5 for columnar and f_s=1.0 for centerline are used to repeat the precipitate calculation, and the results are shown in Figure 10. The particle size is found to significantly increase when segregation is considered, but is still smaller than the experiments. At the center, for example, the calculated particle diameter increases from 4nm without segregation consideration, to 14nm with segregation consideration, which are both quite smaller than the measured diameter 91nm.

The larger observed particles may arise for different reasons. They may be caused by slightly lower temperature than predicted during reheating, which could increase precipitation rate by orders of magnitude. In addition, diffusion is much faster along grain boundaries than in the steel matrix [35], which is neglected in the current model, and the interfacial energy likely changes with temperature during precipitation. More importantly, the current model only computes Nb(C,N) precipitation, but TiN is always much more stable and promotes precipitation in the reheating furnace or even before reheating at a much higher temperature in austenite. Newly formed

Nb(C,N) can precipitate on the surface of large Ti-bearing precipitates to further form coarsened particles. This is consistent with the detection of titanium in most of the larger precipitates in the experiments [17]. These factors help to explain why the current transient precipitate model under-predicts the size distribution. The model is being modified to handle multiple precipitates with variable compositions. More work will be done to better explain and match the measured size in the future.

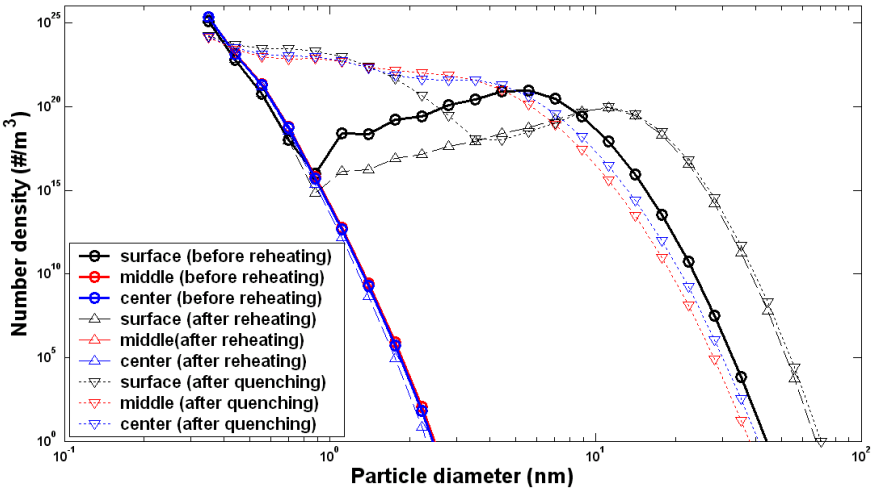

Figure 7: Calculated particle size distribution evolution during processing

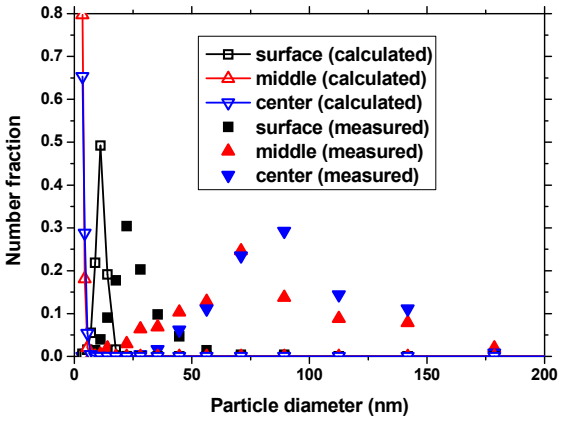

Figure 8: Comparison of calculated and measured precipitate size distribution (no segregation)

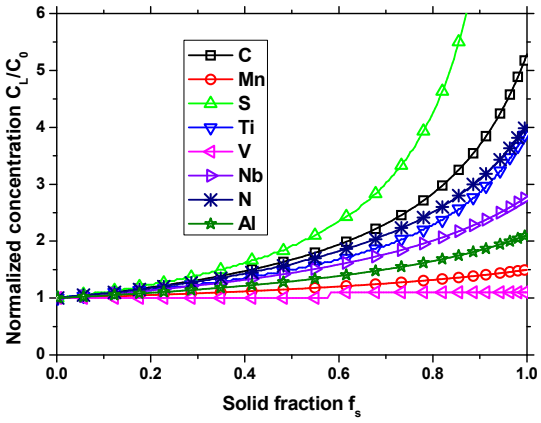

Figure 9: Calculated solute concentrations in the liquid during solidification

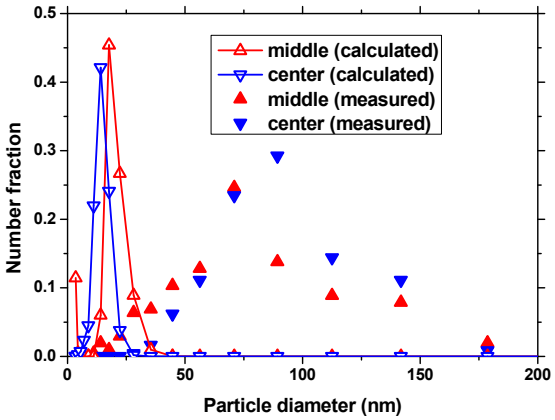

Figure 10: Comparison of calculated and measured precipitate size distribution (with segregation)

Although water quenching is generally thought to be an effective tool to "lock-in" the precipitate properties at high temperature, the current simulation suggests that this may not always be true, especially for the inside of thick samples. This is because precipitation is greatly accelerated during the γ→α phase transformation due to the much lower solubility limits and the much higher diffusion rates in ferrite [13,14]. This agrees with the findings of Simoneau *et al* , who pointed out that a significant fraction of the remaining niobium will precipitate during the γ→α transformation, even for cooling rates as high as 100°C/s [12]. Thus, it is important that minimum-sized samples be taken from an exposed surface of a cropped sample, and that the actual cooling conditions be taken into account via modeling during the analysis phase.

CONCLUSIONS

1. A fundamentally-based model of precipitate formation in practical steel processes has been developed, which includes a heat transfer model for predicting temperature and steel phase histories, an equilibrium precipitation model for predicting the stability and equilibrium amounts and compositions of the precipitate phases, and a kinetic model for predicting the evolution of the precipitate size distribution, including smooth transitions between the nucleation, growth, and coalescence stages.
2. The model predictions of precipitate fraction and amounts agree with measurements conducted on continuous-cast HSLA steel samples taken from a commercial thin-slab caster.
3. The model predictions of precipitate size distribution agree qualitatively but underpredict the measured size distributions, which average 24nm, 72nm, and 91nm in the surface (edge), middle (columnar), and centerline regions of the samples.
4. The simulation gives new insight into precipitate formation for a broader context of HSLA steels, and could also be relevant in the context of slab cracking issues associated with undesired precipitation in slab surface/corner locations. The potential importance of precipitation during specimen acquisition (associated with quenching) is highlighted by the model predictions.

ACKNOWLEDGEMENTS

The authors wish to thank members of the Continuous Casting Consortium at the University of Illinois at Urbana-Champaign (UIUC), sponsors of the Advanced Steel Processing and Products Research Center for their continuous financial support of the research, and Adam J. Shutts at Nucor Hickman, Arkansas, for collecting the samples and help with explaining the experimental conditions.

REFERENCES

1. M. S. Rashid, "High-strength, Low-alloy Steels," *Science*, 1980, vol. 208, pp. 862-869.
2. T. Gladman, *The Physical Metallurgy of Microalloyed Steels*, The Institute of Materials, London, England, 1997.
3. I. Weiss and J. J. Jonas, "Interaction between Recrystallizaiton and Precipitaiton during the High Temperature Deformation of HSLA Steels," *Metallurgical Transactions A*, 1979, vol. 10A, pp. 831-840.
4. J. J. Jonas and I. Weiss, "Effect of Preciptation on Recrystallizaiton in Microalloyed Steels," *Metal Science*, 1979, vol. 13, pp. 238-245.
5. A. J. DeArdo, "Microalloyed Strip Steels for the 21st Century," *Materials Science Forum*, 1998, vols. 284-286, pp.15-26.
6. C. Zener (quoted by C.S. Smith), "Grain, Phases, and Interfaces: an Interpretation of Microstructure," *Transaction of the American Institute Mining and Metallurgical Engineerings*, 1948, vol.175, pp. 15-51.
7. N. Maruyama, R. Uemori and M. Sugiyama, "The Role of Niobium in the Retardation of the Early Stage of Austenite Recovery in Hot-deformed Steels," *Materials Science and Engineering A*, 1998, vol. A250, pp. 2-7.
8. J. G. Speer and S. S. Hansen, "Austenite Recrystallization and Carbonitride Precipitation in Niobium Microalloyed Steels," *Metallurgical Transactions A*, 1989, vol. 20A, January, pp. 25-38.
9. B. G. Thomas, J. K. Brimacombe and I. V. Samarasekera, "The Formation of Panel Cracks in Steel Ingots: a State-of-the-art Review, I. Hot Ductility of Steel," *ISS Transactions*, 1986, vol.7, pp. 7-20.
10. E. S. Szekeres*, Proceedings of 6th International Conference on Clean Steel*, Balatonfüred, Hungary, June 2002, pp. 324-338.
11. B. Mintz, "Influence of Nitrogen on Hot Ductility of Steels and Its Relationship to Problem of Transverse Cracking," *Iron and Steelmaking*, 2000, vol. 27, pp. 343-347.
12. R. Simoneau, G. Bégin and A. H. Marquis, "Progress of NbCN Precipitation in HSLA Steels as Determined by Electrical Resistivity Measurements," *Metal Science*, 1978, vol. 12, pp. 381-386.
13. F. Vodopivec, "Technical Note: on the Influence of Hot Deformation of Low-carbon Steel by Rolling on the Precipitation of Aluminium Nitride," *Journal of The Iron and Steel Institute*, 1973, pp. 664-665.
14. M. Mayrhofer, "Dissolution and Separation Kinetics of Aluminum Nitride in Aluminum Killed Steel," *BHM Berg- und Hüttenmännische Monatshefte*, 1975, vol. 120, pp. 312-321.
15. L. J. Cuddy and J. C. Raley, "Austenite Grain Coarsening in Microalloyed Steels," *Metallurgical Transactions A*, 1983, vol. 14A, pp. 1989-1995.
16. M.G. Akben, I. Weiss, J. J. Jonas, "Dynamic Precipitation and Solute Hardening in a V microalloyed and Two Nb Steels Containing High Levels of Mn," *Acta Metallurgica*, 2081, vol. 29, pp. 111-121.
17. M. S. Dyer, "Study of Microalloy Precipitation in Hot Charged Slabs," *M. S. thesis*, Colorado School of Mines, Golden, CO, 2010.

18. C. P. Reip, S. Shanmugam, and R. D. K. Misra, “High Strength Microalloyed CMn(V-Nb-Ti) and CMn(V-Nb) Pipeline Steels Processed through CSP Thin-slab Technology: Microstructure, Precipitation and Mechanical Properties,” *Materials Science and Engineering,* 2006, vol. A424, pp. 307-317.
19. J. Strid and K. E. Easterling, “On the Solubility and Stability of Complex Carbides and Nitrides in Microalloyed Steels,” *Acta Metallurgica*, 1985, vol.33, pp. 2057-2074.
20. J. G. Speer, J. R. Michael, and S. S. Hansen, "Carbonitride Precipitation in Niobium/Vanadium Microalloyed Steels," *Metallurgical Transactions A*, 1987, vol. 18A, pp. 211-222.
21. M. S. Dyer, J. G. Speer, D. K. Matlock, A. J. Shutts, S. Jansto, K. Xu and B. G. Thomas, “Microalloy precipitation in hot charged slabs,” *Iron and Steel Technology*, 2010, October, pp. 96-105.
22. Y. Meng and B. G. Thomas, “Heat Transfer and Solidification Model of Continuous Slab Casting: CON1D,” *Metallurgical and Materials Transactions B*, 2003, vol. 34B, pp. 685-705.
23. B. Petrus, K. Zheng, X. Zhou, B. G. Thomas, J. Bentsman, “Real-time Model-based Spray-cooling Control System for Steel Continuous Casting,” *Metallurgical and Materials Transactions B*, 2011, Vol. 42B, pp. 87-103.
24. Y. M. Won and B. G. Thomas, “Simple Model of Microsegregation during Solidification of Steels,” *Metallurgical and Materials Transactions A*, 2001, vol. 32A, pp. 1755-1767.
25. K. Xu, B. G. Thomas and R. O’Malley, “Equilibrium Model of Precipitation in Microalloyed Steels,” *Metallurgical and Materials Transactions A*, 2011, vol.42A, pp. 524-539.
26. D. Turnbull and J. C. Fisher, “Rate of Nucleation in Condensed Systems,” *The Journal of Chemical Physics*, 1949, vol. 17, pp. 71-73.
27. C. Zener, “Theory of Growth of Spherical Precipitates from Solid Solution,” *Journal of Applied Physics*, 1949, vol. 20, pp. 950-953.
28. I. M. Lifshitz and V. V. Slyozov, “The Kinetics of Precipitation from Supersaturated Solid Solutions,” *Journal of Physics and Chemistry of Solids*, 1961, vol. 19, pp. 35-50.
29. K. C. Russell, “Nucleation in Solid: the Induction and Steady State Effects,” *Advances in Colloid and Interface Science*, 1980, vol. 13, pp. 205-318.
30. H. I. Aaronson, L. Laird and K. R. Kinsman, “Mechanisms of Diffusional Growth of Precipitate Crystals,” *Phase Transformations*, edited by H. I. Aaronson, 1970, Metal Park, OH, ASM, pp. 313-396.
31. M. Kahlweit, “Ostwald Ripening of Precipitates,” *Advances in Colloid and Interface Science*, 1975, vol. 5, pp. 1-35.
32. L. Kampmann, M. Kahlweit, “On the Theory of Precipitation II, ” *Berichte der Bunsen-Gesellschaft Physikalische Chemie*, 1970, vol. 74, pp. 456-462.
33. T. Nakaoka, S. Taniguchi, K. Matsumoto and S. T. Johansen, “Particle-size-grouping Method of Inclusion Agglomeration and its Application to Water Model Experiments,” *ISIJ international*, 2001, 41, pp. 1103-1111.
34. K. Xu and B. G. Thomas, “Particle-size-grouping Model of Precipitation Kinetics in Microalloyed Steels,” *Submitted to Metallurgical and Materials Transactions A*.
35 J. Geise and C. Herzig, “Lattice and Grain Boundary Diffusion of Niobium in Iron,” *Zeitschrift fur Metallkunde*, 1985, vol. 76, pp. 622-626.